nature sensors

Article

https://doi.org/10.1038/s44460-025-00018-8

Quantized Landau-level crossing checkerboards for cryogenic magnetometry

Received: 15 May 2025

Accepted: 11 December 2025

Published online: 20 January 2026

Check for updates

Baojuan Dong[1,2,3,4,11], Kai Zhao[1,2,11], Ze Wang[5], Chuanying Xi[5], Changhao Zhao[6], Kenji Watanabe[7], Takashi Taniguchi[8], Jianming Lu[4], Jianting Zhao[6] ✉, Fengcheng Wu[9,10] ✉, Jing Zhang[1,2,3] ✉ & Zheng Vitto Han[1,2,4] ✉

When charge transport occurs under conditions such as topological protection or ballistic motion, the conductance of low-dimensional systems often exhibits quantized values in units of e^2/h, underpinning advances in quantum metrology and computing. Here we report a quantized quantity: the ratio of displacement field to magnetic field, D/B, in large-twist-angle bilayer graphene. In high magnetic fields, Landau-level crossings between the top and bottom layers produce equal-sized checkerboard patterns across the D/B–ν space. These arise from electric-field-driven interlayer charge transfer of one elementary charge per flux quantum, yielding quantized critical displacement intervals, $\delta D = \frac{e}{2\pi l_B^2}$, where l_B is the magnetic length. This mechanism offers a route to magnetic sensing, as the displacement-to-magnetic-field ratio is defined solely by fundamental constants. We propose a prototype magnetometer based on this principle, potentially enabling planar mapping of magnetic fields with micrometre resolution via large-twist-angle bilayer graphene sensor arrays. Our results demonstrate that interlayer charge transfer in the quantum Hall regime gives rise to novel phenomena with potential applications in cryogenic magnetometry.

In a low-dimensional quantum conductor, charge transport often exhibits discrete characteristics, sometimes appearing as staircases of plateaux under varying magnetic or electric fields, in units of either the superconducting flux quantum, defined as $\Phi_0 = \frac{h}{2e}$, or conductance quantum defined as $G_0 = \frac{e^2}{h}$. However, up to now, only a few candidates in solid states can manifest quantized physical measurables, including the conductance of quantum point contacts[1–4], Shapiro voltage steps in Josephson junctions[5,6] and the conductance of topologically non-trivial electronic phases such as quantum Hall or Chern insulators[7–10]. These simple yet elegant kinds of quantization have found key applications in modern quantum technologies such as quantum metric standards[11–14], as well as quantum information processing[15]. Exploring previously unexplored systems that may exhibit quantities with quantization (or quantized jumps) is thus of fundamental importance and holds great promise for applications based on exotic quantum states.

Among the reported low-dimensional systems, interlayer charge transfer in large-angle (LA) twisted graphene in the quantum Hall

[1]State Key Laboratory of Quantum Optics Technologies and Devices, Institute of Optoelectronics, Shanxi University, Taiyuan, People's Republic of China. [2]Collaborative Innovation Center of Extreme Optics, Shanxi University, Taiyuan, People's Republic of China. [3]Hefei National Laboratory, Hefei, People's Republic of China. [4]Liaoning Academy of Materials, Shenyang, People's Republic of China. [5]Anhui Province Key Laboratory of Condensed Matter Physics at Extreme Conditions, High Magnetic Field Laboratory of the Chinese Academy of Science, Hefei, People's Republic of China. [6]Division of Electrical and Magnetic Metrology, National Institute of Metrology, Beijing, People's Republic of China. [7]Research Center for Electronic and Optical Materials, National Institute for Materials Science, Tsukuba, Japan. [8]Research Center for Materials Nanoarchitectonics, National Institute for Materials Science, Tsukuba, Japan. [9]School of Physics and Technology, Wuhan University, Wuhan, People's Republic of China. [10]Wuhan Institute of Quantum Technology, Wuhan, People's Republic of China. [11]These authors contributed equally: Baojuan Dong, Kai Zhao. ✉e-mail: zhaojt@nim.ac.cn; wufcheng@whu.edu.cn; jzhang74@sxu.edu.cn; vitto.han@gmail.com

regime has attracted interest. In this system, as the layer-dependent chemical potential is tuned by varying the vertical electric field at a fixed filling fraction ν, charges from the bottom (top) graphene layer migrate to the top (bottom) layer[16–19]. Nevertheless, previous experimental observations have been limited to relatively low magnetic fields, with few details explored within the Landau-level (LL) crossings. As a result, potentially sophisticated features may have been missed, since the spin and valley degeneracies remain unresolved in this regime[16–18,20]. Recently, twisted graphene systems with both small and moderate angles have been investigated[17,19,21–27]. In twisted bilayer graphene (TBLG) with twist angles close to the so-called magic angle of 1.1°, flat-band physics is observed[21,22,24,25], whereas twisted double bilayer graphene systems with moderate twist angles of approximately 2–10° do not exhibit flat bands but instead display tunable excitonic insulating phases[17,19,26,27]. Electronic transport in TBLG with large twist angles, such as 30°, has also been reported in chemical vapour deposition samples[20,28,29].

In this work, we show that, by stacking two layers of graphene with a large twist angle (20–30°), specific equal-sized checkerboard patterns can be observed in the quantum Hall regime at the LL crossings throughout the D–n space, when all spin- and valley-flavour degeneracies are lifted. Our experimental and theoretical investigations reveal that this quantized 4 × 4 checkerboard feature originates from the critical electric displacement field D, which bridges the phase transition of two different charge filling states in the TBLG at LL crossings. This phase transition results from competition between the layer polarization driven by the D field and the capacitance coupling energy, while the charge transfer at LL crossings, driven by vertical electrical fields, corresponds to exactly one elementary charge transferred between the top and bottom Landau orbits. Therefore, at a fixed ν, varying D will lead to LL crossings equally spaced by an interval of $\delta D = \frac{e}{2\pi l_B^2} = Be^2/h$. We can thus define a measurable, the ratio of D/B, which displays quantization of e^2/h in the LL-crossing checkerboard. Our findings suggest a new paradigm of magnetic sensing, as the displacement-to-magnetic field ratio in such LL-crossing quantized checkerboards can be scaled in a linear B–δD relation. A prototype of this magnetometer is demonstrated, which could be further developed into sensor arrays for high-spatial-resolution surface magnetometry in the future.

Results and discussion

Fabrications and characterizations of LA-TBLG devices

Monolayered graphene and few-layered hexagonal boron nitride (h-BN) flakes were exfoliated from bulk crystals. The graphene was cut by a conductive atomic force microscope tip, using the anode-oxidation technique[30,31]. The graphene twin flakes, cut using an atomic force microscope, were stacked with a twist angle of 20° or 30° via the dry transfer method[32] and then encapsulated by top and bottom h-BN flakes. Detailed fabrication processes can be seen in Supplementary Figs. 1–3. The devices were equipped with dual gates and electrodes of Ti/Au via standard lithography and electron-beam evaporation (for fabrication details, see Methods), as illustrated in Fig. 1a. Figure 1b shows the optical micrograph of a typical LA-TBLG device (Sample-S15, 30°-twisted), with the corresponding fabrication flow shown in Supplementary Fig. 2. Before further analysis, we define the two-gate-induced displacement field as $D = (C_{tg}V_{tg} - C_{bg}V_{bg})/2 - D_r$, and the total carrier density as $n_{tot} = (C_{tg}V_{tg} + C_{bg}V_{bg})/e - n_r$, as commonly used in dual-gated graphene devices[33,34]. Here, C_{tg} and C_{bg} are the top and bottom gate capacitances per area, respectively, and V_{tg} and V_{bg} are the top and bottom gate voltages, respectively. n_r and D_r are the residual doping and residual displacement field, respectively. Figure 1c shows a mapping of longitudinal resistance R_{xx} of Sample-S15 in the D–n space, when cooled down to T = 1.5 K at B = 0 T. It is noteworthy that, along the charge neutral line (carrier density n = 0), R_{xx} decreases when D is departing from zero. This behaviour reflects the weak interlayer coupling[16], which markedly distinguishes it from conventional strongly coupled Bernal-stacked bilayer graphene systems. In the latter, R_{xx} at charge neutrality monotonously increases upon increasing the absolute value of D, due to the gap opening at the Dirac point[35,36]. Data from a control sample of Bernal-stacked bilayer graphene are presented for comparison in a side-by-side format in Supplementary Fig. 4.

Figure 1d illustrates the mapping of R_{xx} (in a log scale for visual clarity) in the D–n space within the same range of Fig. 1c at B = 5 T. Resistive states (circular-shaped dots) are clearly observed at each LL crossing on both the electron and hole sides, with each dot exhibiting a non-uniform size distribution. This is consistent with previous observations in a weakly coupled TBLG sample, for which the twist angle was not reported[16]. Note that all LL crossings here exhibit fourfold degeneracy, as can be seen in the transverse conductance σ_{xy} in Supplementary Fig. 5, when plotted in the D–n space. Hence, all the crossing points can be marked by $[N_b, N_t]$, where the N_b and N_t represent the LL indices for the bottom and top graphene layers, as shown in Supplementary Fig. 5b.

When further increasing the perpendicular magnetic field, spin and valley degeneracy start to be lifted, and the single-dot-shaped resistive states in the D–n space at low B develop into 4 × 4 matrices. The newly developed LL crossings can be labelled by (ν_b, ν_t), within a given $[N_b, N_t]$, where $\nu_{b,t}$ is the filling fraction of each layer. Surprisingly, it is observed that all 4 × 4 checkerboard cells exhibit the same uniform size throughout the D–n space, regardless of their parent index $[N_b, N_t]$, which is the central finding of this work, as shown in Fig. 1e,f. Here, Fig. 1e is the theoretical simulation that agrees well with the experimental data in Fig. 1f. The x and y axes of Fig. 1e,f are linearly transformed from n to ν, and from D to D/B, respectively. We notice that some of the checkerboards are less clearly observed at certain areas of n and D, which is due to contact issue of the as-fabricated devices. More theoretical details will be discussed in the coming sections. In another typical LA-TBLG device (Sample-S37, 20°-twisted), we carried out high-resolution mapping of R_{xx} in the D-ν space, at $[N_b, N_t]$ = [1, 2] (Fig. 1f, dashed red box), for different magnetic fields. As shown in Fig. 1g–j, the evolution from the single-dotted to 4 × 4 checkerboard-like LL crossings can be clearly seen, from 2 T to 8 T, which is consistent with the observations in Sample-S15, as shown in Supplementary Fig. 6. We show in Supplementary Figs. 7–9 other tested LA-TBLG samples.

Quantized D/B jumps

In this study, we mainly focus on the physical origin of the equally sized checkerboard patterns at the LL crossing, taking the $[N_b, N_t]$ = [1, 2] checkerboard as an example for examination. The displacement field used in all the figures and discussions has been corrected by using the decoupled interlayer model, taking into account the sample-dependent interlayer quantum capacitance C_{GG} (which largely influences the calculated D) of the TBLG[16]. In Supplementary Note 1 and Supplementary Fig. 10, we show that, using the decoupled TBLG model[16], C_{GG} can be fitted to be 6.30 μF cm^{-2} for Sample-S37. As a comparison, C_{GG} of Sample-S15 is also calibrated in Supplementary Fig. 10. Figure 2a,b plots the line profiles of σ_{xy} and R_{xx} along dashed black and red lines in Fig. 2c, while the same colour codes are used for the line profiles. At D/ε_0 = 0.3493 V nm^{-1} (outside the checkerboard), spin and valley degeneracies are fully lifted, with all integer quantum Hall states from filling 8 to 16 observed as quantized conductance plateau in σ_{xy}, and corresponding resistance minima in R_{xx}. Meanwhile, at D/ε_0 = 0.4726 V nm^{-1} (centre of the checkerboard), only even-integer quantum Hall states are seen in σ_{xy}. The odd integer fillings are occupied by the resistive states at LL crossings.

Interestingly, when scaling the displacement field into D/B, all the resistive states at LL crossings are found to be located at a quantized value in the $(D - D_0)/B$ axis with respect to the centre of the checkerboard, in units of $e^2/2h$. This effect can be more pronounced when

https://doi.org/10.1038/s44460-025-00018-8

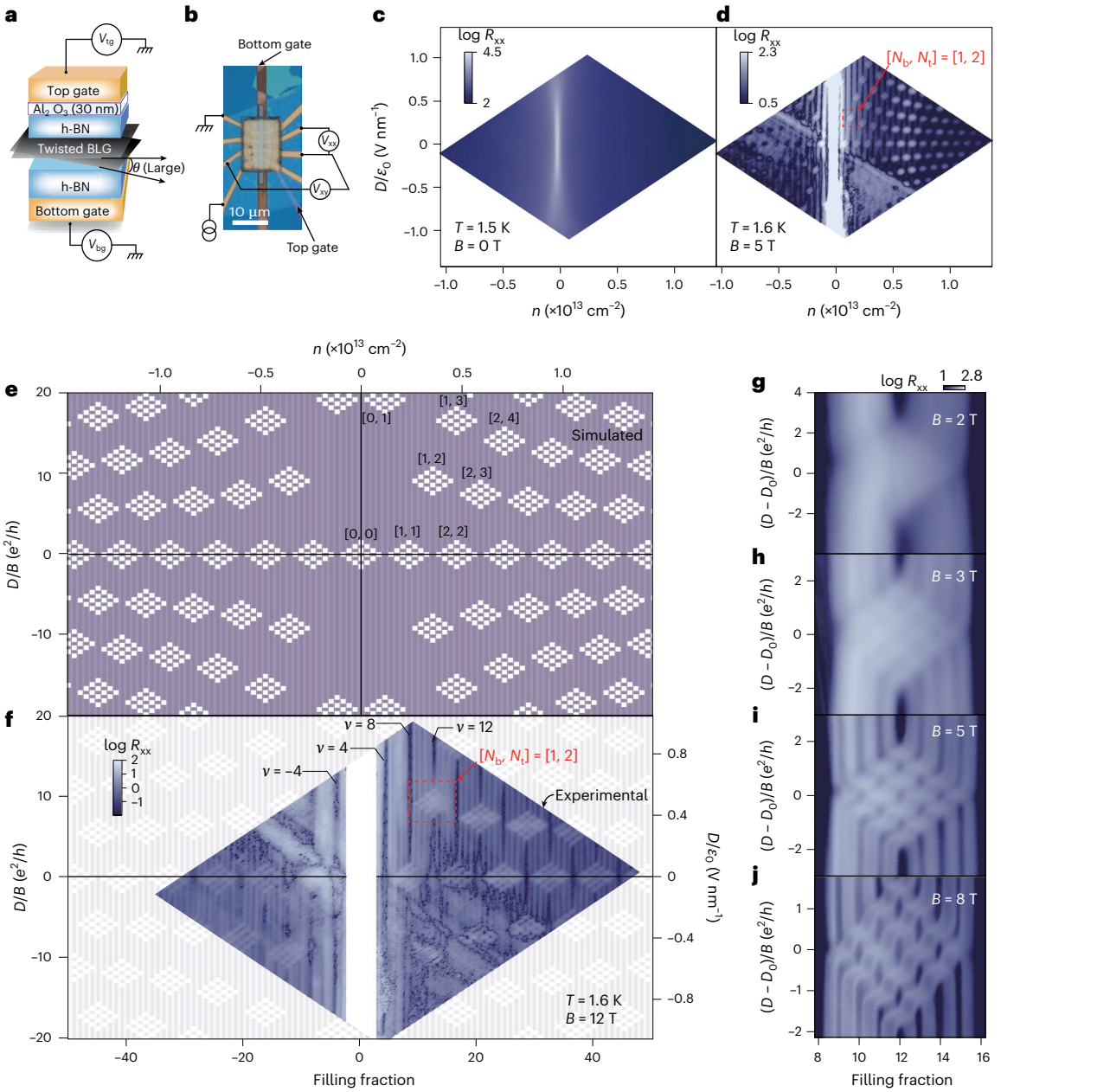

Fig. 1 | Equal-sized checkerboard cells at LL crossings in the *D*–*n* space in LA-TBLG. a, A schematic illustration of the device. **b**, An optical image of a typical LA-TBLG device (Sample-S15, 30°-TBLG). Notice that a larger top gate is applied to diminish the parasitic contact doping effects. **c**,**d**, R_{xx} mapping in the *D*–*n* space of Sample-S15 at $T = 1.5$ K and $B = 0$ T (**c**) and $T = 1.6$ K and $B = 5$ T (**d**) (in a log scale for visual clarity). **e**,**f**, Simulated (**e**) and experimental (**f**) checkerboard patterns at LL crossings in the weak layer coupling regime of TBLG at $B = 12$ T in the *D*–*n* space. Notice that a background of simulated patterns is overlaid on top of experimental data in **f**, as a visual guide. The dashed red box indicates LL crossings of $[N_b, N_t] = [1, 2]$. Typical filling factions of $\nu = \pm 4$, 8 and 12 are labelled. R_{xx} is truncated at a maximum value of 100 Ω, appearing white at the charge neutrality point. **g**–**j**, The evolution from the single-dotted to 4 × 4 checkerboard-like LL crossings at $[N_b, N_t] = [1, 2]$, at $B = 2$ (**g**), 3 (**h**), 5 (**i**) and 8 (**j**) T. Data were obtained at $T = 1.6$ K.

plotted as line profiles along $\nu = 12$ of both R_{xx} and σ_{xy}, with the *y* axes shifted to the centre of the checkerboard, noted as $(D - D_0)/B$, shown in Fig. 2d. We also rescaled all the *y* axes into D/B for Fig. 1e–f, or $(D - D_0)/B$ for Fig. 1g–j, respectively.

In the LL-crossing checkerboard plotted in the parameter space of $(D - D_0)/B$ and filling fraction ν, two types of quantized properties can be observed, with one of them being the well-known quantum Hall effect-originated quantization of filling fractions and the other being the interval in $(D - D_0)/B$ for R_{xx} peaks, as indicated by the arrows in Fig. 2c. We now provide a theoretical explanation for this observation. For low-energy electrons, our current system can be approximated by two layers that are decoupled at the single-particle level because of the large twist angle, but capacitively coupled by Coulomb interaction. Due to the spin and valley degeneracies within each graphene layer, the filling factor ν_i and LL index N_i have the following relation: $\nu_i = 4N_i - 2 + \tilde{\nu}_i$, where *i* is the layer index, $\tilde{\nu}_i$ is the filling factor of the partially filled LL with index N_i, and $0 \leq \tilde{\nu}_i \leq 4$. Hence, the filling factor within the LL-crossing checkerboard indexed by $[N_b, N_t]$ can be an integer number between $4(N_b + N_t) \pm 4$, also written as $\nu = \nu_b + \nu_t = 4(N_b + N_t - 1) + \tilde{\nu}$, where $\tilde{\nu} = \tilde{\nu}_b + \tilde{\nu}_t$. We construct the total energy per area (defined as E_{tot}), which comprises three terms: the single-particle energy of the occupied LLs, the classical electrostatic energy (including the layer potential difference generated by the *D* field and the capacitance energy) and the intralayer exchange energy,

https://doi.org/10.1038/s44460-025-00018-8

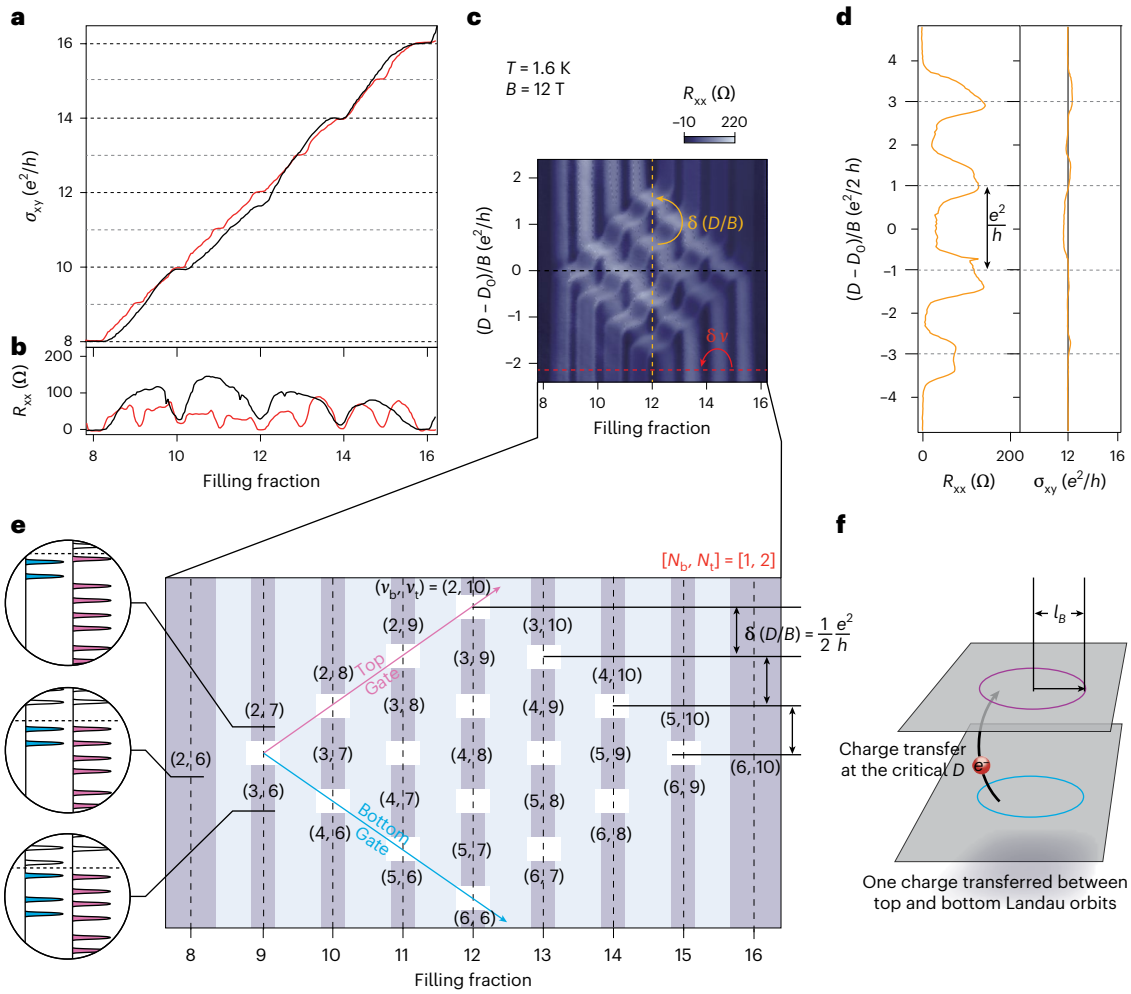

Fig. 2 | Quantized D/B jumps of interlayer charge transfer phase transition at fixed ν in the LL-crossing area of $[N_b, N_t] = [1, 2]$. a,**b**, Line profiles of σ_{xy} (**a**) and R_{xx} (**b**) along dashed black and red lines in **c**. The same colour codes are used for the solid lines in **a** and **b**, and the dashed lines in **c**. **c**, The y axis of the colour mapping of R_{xx} is plotted in both raw D (right; corrected according to Supplementary Fig. 10 and Supplementary Note 1) and $(D - D_0)/B$ (left), where D_0 is defined as the central D of the checkerboard. When plotted as $(D - D_0)/B$, adjacent LL crossings are observed to be separated by a quantized value of e^2/h when ν is fixed. **d**, Line profiles along $\nu = 12$, that is, the dashed orange line in **c**, of R_{xx} and σ_{xy}, respectively. **e**, A drawing of the quantized 4 × 4 checkerboard at the LL crossing of $[N_b, N_t] = [1, 2]$. The fillings of Landau bands for (2, 6), (3, 6) and (2, 7) are schematically illustrated on the left. **f**, A cartoon illustration for the event of charge transfer at critical D for any phase boundaries (marked as white boxes) along fixed ν in **e**.

as described in Methods. Theoretically, we assume that the integer quantum Hall insulators are formed within each layer, neglecting the interlayer exchange interaction and Zeeman energy (the subtle effects of spin ordering and Zeeman effect are discussed in Methods).

In the LL-crossing checkerboard indexed by $[N_b, N_t]$, the states at a fixed ν can change from one phase $\{N_b, \tilde{\nu}_b; N_t, \tilde{\nu}_t\}$ to another adjacent one $\{N_b, \tilde{\nu}_b - 1; N_t, \tilde{\nu}_t + 1\}$ driven by the displacement field, leading to a phase transition that yields discrete phase boundaries (corresponding to experimentally observed resistive peaks at a given ν in the checkerboards). The critical displacement field can then be found at the conditions when the energies of the above two adjacent filling phases become degenerate, as shown in Methods. Solving them, one can obtain all the critical field $\tilde{D} = \frac{D}{en_0} = \frac{D}{B}/(\frac{e^2}{h})$ in each checkerboard to be 0, ±1/2, ±1 and ±3/2 measured relative to the centre of the checkerboard, as given in the third column in Table 1. At this stage, it is clear that $\delta D/B$ between each adjacent phase boundary at fixed ν is quantized to e^2/h. As our theory shows, the value of $\delta D/B$ within a checkerboard is fully determined by the competition between the D-field-driven layer potential difference and the Coulomb-driven capacitance energy, where the former (latter) favours layer polarization (equal charge distribution between the two layers), which makes $\delta D/B$ independent of the parent index $[N_b, N_t]$. As integer quantum Hall insulators are incompressible with an integer number of electrons per flux quantum, the charge transfer at the crossings is exactly one charge per Landau orbit of area $2\pi l_B^2$, making δD quantized to $\frac{e}{2\pi l_B^2}$. Using the experimentally extracted C_{GG}, we plot the full map of checkerboards in the space of D/B and ν in Fig. 1e (and the background in Fig. 1f), which agrees well with experimental results.

Figure 2e illustrates the theoretical picture discussed above, taking the LL crossing indexed by $[N_b, N_t] = [1, 2]$ as an example. White boxes denote the phase boundaries at which the states change along the vertical direction (that is, the fixed ν), driven by the displacement field. For the three filling states $(\nu_b, \nu_t) = (2, 6)$, (3, 6) and (2, 7), LLs alignments for each layer are illustrated in the circled schematics (blue and pink colour denote LLs for bottom and top layers, respectively). Those white boxes form an evenly distributed matrix with 4 × 4 elements, due to the quantization of both ν in the x axis, and D/B in the y axis, respectively. The latter quantization of the measurable D/B within a checkerboard at LL crossing was not quantitatively established before, although similar matrices of resistive peaks in LL crossing of twisted graphene have been

https://doi.org/10.1038/s44460-025-00018-8

Table 1 | Critical displacement fields for $\tilde{v} = 1, 2, 3, 4$

$\tilde{v} = \tilde{v}_b + \tilde{v}_t$	$(\tilde{v}_b, \tilde{v}_t) \leftrightarrow (\tilde{v}_b - 1, \tilde{v}_t + 1)$	$\tilde{D}^{(c)}_{N_b,N_t} - \tilde{D}^{(0)}_{N_b,N_t}$
1	(1, 0) ↔ (0, 1)	0
2	(2, 0) ↔ (1, 1)	$-\frac{1}{2}$
	(1, 1) ↔ (0, 2)	$+\frac{1}{2}$
3	(3, 0) ↔ (2, 1)	−1
	(2, 1) ↔ (1, 2)	0
	(1, 2) ↔ (0, 3)	+1
4	(4, 0) ↔ (3, 1)	$-\frac{3}{2}$
	(3, 1) ↔ (2, 2)	$-\frac{1}{2}$
	(2, 2) ↔ (1, 3)	$+\frac{1}{2}$
	(1, 3) ↔ (0, 4)	$+\frac{3}{2}$

The critical fields for $\tilde{v} = 5, 6, 7$ are the same as those for $\tilde{v} = 3, 2, 1$, respectively.

reported elsewhere[19]. Charge transfer between LLs in a two-subband system of double quantum wells was also investigated; however, the quantization signature reported here was not observed there[37]. In the experiment, the two solid blue and pink arrows in Fig. 2e indicate the sweeping direction in terms of bottom and top gates, respectively (see also Supplementary Fig. 6d). The quantization of $\delta D/B$ is thus a manifestation of the well-defined interlayer distance in LA-TBLG with well-developed quantum Hall ferromagnetism of spin and valley ordering, studied in the current work. Figure 2f illustrates a cartoon drawing that depicts the observed phenomena using a simplified representation of charge transfer between LLs. The density per Landau orbit area is written as $\delta n = eB/h$, while the charge change is also defined according to the capacitance coupling by $e\delta n = \delta D$. Taking the above two relations, one obtains $\delta D/B = e^2/h$.

We further investigate the B and T dependencies of D/B quantizations at fixed v within one quantized checkerboard. Figure 3a depicts the line profiles of R_{xx} for v from 9 to 15, for the checkerboard at LL crossing of $[N_b, N_t] = [1, 2]$ measured in Sample-S37 at $T = 1.6$ K and $B = 12$ T (the same analysis of Sample-S15 can be found in Supplementary Fig. 11). These resistive peaks at critical D can be fitted using the Gaussian distribution, and hence the distance between each pair of adjacent peaks can be determined as $\delta D/B$. We plot the R_{xx} at $v = 12$ as a function of magnetic fields, as shown in Fig. 3b. It can be seen that, at relatively low magnetic fields, the LL crossings still appear as a single dotted resistive peak, as no degeneracy lifting has occurred. Above about 3 T, a clear four-peak feature can be observed in the line profile, and peaks are well developed at about 5 T. Figure 3c illustrates the measured $\delta D/B$ (in units of e^2/h) as a function of magnetic field, and the experimental data distribute around the unity, which is expected according to our theoretical modelling. The data in Fig. 3c are derived from the statistical analysis of nine $\delta D/B$ values, as detailed in Supplementary Tables 1 and 2. More data on the temperature dependence of $(D - D_0)/B$ are given in Supplementary Fig. 12.

Tuning the LL-crossing checkerboard with Zeeman energy

At this stage, it is noticed that the uniform 4 × 4 matrix checkerboard patterns were observed in only a small fraction of (fewer than 1/10) the as-fabricated samples, including Sample-S15 and Sample-S37. As shown in Supplementary Figs. 9–11, the checkerboard patterns in other samples were distorted, where these resistive states (crossing points in the 4 × 4 matrix) are divided into four subgroups. Our theory described in Methods, which assumes spin conservation in the charge transfer, is found to match well with the data for uniform 4 × 4 matrix checkerboards. However, different samples may exhibit different spin orderings due to the competition between Zeeman energy and the atomic-scale interactions. To examine the Zeeman effect, we performed tilted-field magnetotransport of Sample-S37. As illustrated in Supplementary Fig. 13a, the LA-TBLG sample is subjected to a tilted field, while the total magnetic field (B_{tot}) is increased with $B_\perp$ held constant. The in-plane projection $B_\parallel = B_{tot} \sin\varphi$ can thus effectively tune the Zeeman energy in the tested system, where φ is the angle of tilt.

As shown in Supplementary Fig. 13b–d, at a fixed index of $[N_b, N_t] = [1, 2]$ and a constant $B_\perp = 5$ T at $T = 1.6$ K, the 4 × 4 matrix checkerboard is tuned from its initial uniform distribution (Supplementary Fig. 13b, $\varphi = 0°$) into gradually distorted patterns (Supplementary Fig. 13c, $\varphi = 45°$). For the case of $\varphi = 65°$ in Supplementary Fig. 13d, the checkerboard is clearly divided into four subgroups, with the differences between adjacent R_{xx} in the axis of $(D - D_0)/B$, defined as $\delta D/B$, developing into two typical values, marked as δ_1 and δ_2, respectively, as indicated in Supplementary Fig. 13e. Line profiles of R_{xx} against $(D - D_0)/B$ at $v = 12$ for the case of tilted field angle $\varphi = 0°$ (red line) and $\varphi = 65°$ (green line) are plotted in Supplementary Fig. 13e, with the R_{xx} value shifted for visual clarity. With the in-plane magnetic field $B_\parallel$ varied from zero (red) to 10.72 T ($\varphi = 65°$, green), the value of δ_2 is almost doubled. Supplementary Fig. 13f further plots $\delta D/B$ as a function of φ. While δ_2 increases drastically with the tilt angle, δ_1 remains remarkably quantized at e^2/h. This is direct evidence that the checkerboard pattern can be effectively influenced by tuning the Zeeman energy in the system. Despite this influence, the quantization of $\delta D/B$ in e^2/h can still be manifested, for example, through δ_1. Further detailed theory that takes into account different spin orders will be needed to quantitatively describe such subtle behaviours.

Finally, we show a potential application using the phenomenon of uniform 4 × 4 matrices of quantized LL-crossing checkerboards for LA-TBLG devices. Magnetometers can be classified into weak-field sensors (superconducting quantum interference device, nitrogen–vacancy centres, fluxgates and so on) that maximize fT-pT/$\sqrt{\text{Hz}}$ sensitivity in near-zero backgrounds—often needing shielding and offering limited dynamic range—and strong-field sensors (vibrating sample magnetometer, Hall sensors, nuclear magnetic resonance pickup coils and so on) that operate inside multi-tesla static or pulsed magnets, prioritizing range and robustness over ultimate sensitivity[38,39]. In our study, the proposed sensor uniquely combines scalable on-chip integration and micrometre-scale spatial resolution for sensing ultrahigh B-fields (can be above 30 T) under cryogenic conditions.

When plotting the magnetic field B in tesla against δD with a unit of C m^{-2}, the slope should correspond to the von Klitzing constant h/e^2. Intriguingly, such a linear dependence of B–δD can, in principle, be further used as a kind of quantum magnetometer. Interestingly, these micrometre-sized magnetometric sensors (Fig. 4a), incorporating LA-TBLG, can be readily integrated into an on-chip sensor arrays, as illustrated in Fig. 4b. This further enables surface magnetic field mapping at millimetre-to-centimetre scales (Fig. 4c). One potential application is the spatial calibration of high magnetic fields, such as within the spherical region of a superconducting coil. Naturally, implementing the wiring to connect each Hall bar in such an array would require algorithms and data acquisition hardware, which represents a challenging engineering task beyond the scope of the current study and is left for future work. Albeit challenging, recent studies suggest that twisted-graphene films obtained by chemical vapour deposition[23] would be a possible route to realize large-scale arrays of LA-TBLG devices illustrated in Fig. 4a.

As a proof of concept, we calibrated a typical B-to-δD slope using experimental data at relatively low B, as shown in Fig. 4d. Such a calibrated device can then be utilized as a sensor for measuring unknown B at high B and low T, by simply reading the δD in the quantized LL-crossing checkerboard. Regarding the sensitivity of magnetic field strength, we provide an initial estimation based on noise measurements of our device under fixed experimental conditions. As shown in

https://doi.org/10.1038/s44460-025-00018-8

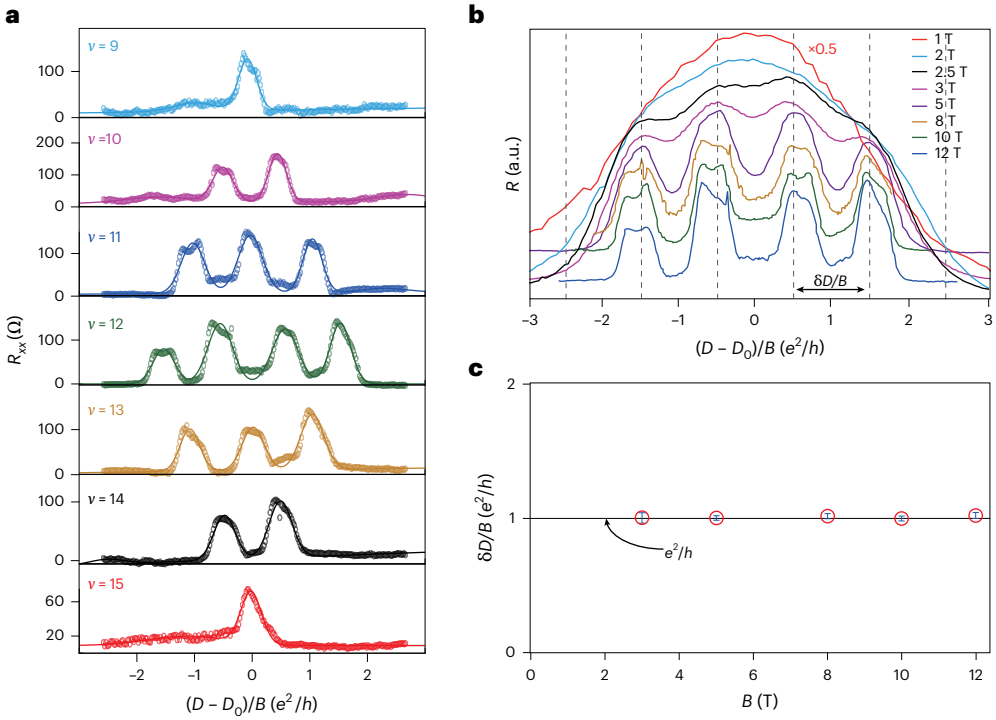

Fig. 3 | Magnetic field dependence of D/B quantizations at fixed ν in the LL-crossing area of $[N_b, N_t] = [1, 2]$. a, The line profiles of R_{xx} at 1.6 K with 12 T magnetic field at filling factors ν from 9 to 15, which were fitted using the Gaussian method to extract the precise crossing R_{xx} peak positions in the checkerboard. **b**, R_{xx} at $\nu = 12$ as a function of $(D - D_0)/B$ at different magnetic fields from 1 T to 12 T. Data are shifted on the y axis for visual clarity. **c**, The statistics of $\delta(D/B)$ as a function of magnetic field. Quantization at e^2/h of $\delta(D/B)$ is clearly seen in **b**. Error bars in **c** are defined as the standard error of the mean of nine values of $\delta(D/B)$ at each magnetic field.

Supplementary Figs. 14–17 and Supplementary Table 3, the uncertainty in our device is estimated to be 0.68% at 20 T, and 1.06% at 30 T, respectively. In the language of weak-field sensing, the measured noise floor allows us to infer a magnetic field sensitivity at the order of approximately 0.1 – 0.4 T/$\sqrt{\text{Hz}}$ for B ranging from 3 T to 30 T. This level of sensitivity, although not fully optimized, demonstrates the potential of our device for applications in high-field magnetometry.

To conclude, we have devised a system of LA (20°–30°) TBLG, in which equal-sized 4 × 4 checkerboards are seen at each interlayer LL-crossing point throughout the D–n parameter space, when all spin- and valley-flavour degeneracies are lifted. When looking into one of such checkerboards in the D–n (or D/B–ν) space, in addition to the well-known quantum Hall effect-driven quantized properties on the ν axis, varying D at a fixed integer filling fraction ν will also yield quantized distance between resistance peaks in the D/B axis in a unit of e^2/h. Such quantization of $\delta D/B$ originates from the charge quantization per Landau orbit of integer quantum Hall states. The intriguing linear relationship between magnetic field B and intervals of critical displacement fields δD, with a slope equal to the conductance quantum, in LA-TBLG-based devices may be exploited as a cryogenic magnetometer beyond conventional approaches. For example, it can be scaled up into sensor arrays to map in-plane magnetic field distributions with micrometre-scale spatial resolution, limited in principle by the device size. The self-calibrating nature of the LL-crossing checkerboards enables low-field calibration, as well as high-field sensing through a δD readout process.

Methods

Sample fabrication

Van der Waals few-layer structures of the h-BN/graphene/h-BN sandwich were obtained by mechanically exfoliating high-quality bulk crystals. The vertical assembly of these van der Waals layered compounds was fabricated using a dry-transfer method under ambient conditions. The h-BN/graphene/h-BN sandwich was then transferred onto the prefabricated h-BN/Au substrate. Hall bars of the devices were achieved by reactive ion etching. During the fabrication processes, electron beam lithography was performed using a Zeiss Sigma 300 SEM with a Raith Elphy Quantum graphic writer. One-dimensional edge contacts were achieved using electron beam evaporation. After atomic layer deposition of about 30 nm Al_2O_3, a big top gate was deposited to form the complete dual-gated h-BN-encapsulated LA-TBLG devices as shown in Fig. 1a,b. Gate and contact electrodes were fabricated by electron beam evaporation, with typical Au/Ti thicknesses of ≈30/5 nm and ≈50/5 nm, respectively.

a.c. electrical measurements

During measurements, the graphene layers were fed with an a.c. I_{bias} of about 50–500 nA. The longitudinal and Hall voltages were recorded using low-frequency SR830 lock-in amplifiers. Four-probe measurements were used throughout the transport measurements under a high magnetic field and at low temperatures in an Oxford TeslaTron cryostat. Gate voltages on the as-prepared Hall bar devices were maintained by a Keithley 2400 source meter.

High-magnetic-field facility

A water-cooled magnet with maximum of 30 T magnetic field and base temperature of 1.7 K was used. The facility is equipped with a water-cooling system and is maintained by the Steady High Magnetic Field Facilities at the High Magnetic Field Laboratory, Chinese Academy of Sciences.

Theory of LL-crossing checkerboards

Energetics. We formulate the energy of the LA-TBLG in a strong magnetic field. Because of the large twist angle, the low-energy electronic states of the two layers can be described by decoupled Dirac fermions at the single-particle level. In the presence of the magnetic field, the

https://doi.org/10.1038/s44460-025-00018-8

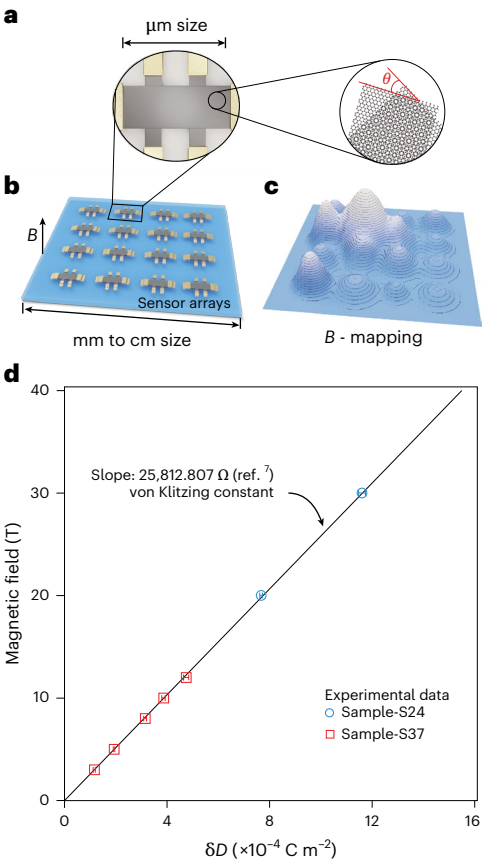

Fig. 4 | Quantized LL-crossing checkerboards as cryogenic magnetometric sensors. a, Schematic of a typical LA-TBLG sample, with the twist angle illustrated in a side inset. **b**, The proposed magnetometric sensor consisting an array of LA-TBLG devices (as shown in **a**), scalable from millimetres to centimetres, operating under a perpendicular magnetic field B. **c**, Schematic representation of magnetic field mapping using cryogenic magnetometric sensor arrays (as in **b**), with equipotential lines schematically drawn, indicating the potential capability of surface mapping of magnetic fields. **d**, The magnetic field B plotted against δD (in C m^{-2}). The slope is then equal to the von Klitzing constant. This linear dependence of B–δD, once calibrated using experimental data at relatively low B, can then be used as cryogenic magnetometric sensors to measure unknown B at high B and low T, by reading the δD in the quantized LL-crossing checkerboard. Error bars in **d** are defined as the standard error of the mean of δD. The error bars for the 3–12 T are obtained from 9 δD of Sample-S37 at each field, and the error bars for 20 T and 30 T are estimated from the 14 and 6 δD of Sample-S24, respectively.

Dirac fermions form quantized LLs. We denote the LL filling factor of the i layer as ν_i, where i = b and t, respectively, for the bottom (b) and top (t) layer. We use N_i to label the index of the partially filled LL nearby the Fermi energy in the i layer. Given the spin and valley degrees of freedom within each graphene layer, ν_i and N_i have the following relation:

$$\nu_i = 4N_i - 2 + \tilde{\nu}_i, \tag{1}$$

where $\tilde{\nu}_i$ is the filling factor of the partially filled LL with index N_i, and $0 \le \tilde{\nu}_i \le 4$.

The electron density of the i layer is $n_i = \nu_i n_0$. Here, n_0 is the electron density per LL given by

$$n_0 = \frac{1}{2\pi l_B^2} = \frac{eB}{h}, \tag{2}$$

where $l_B = \sqrt{\hbar/(eB)}$ is the magnetic length.

The total filling factor is

$$\nu_{\mathrm{tot}} = \nu_\mathrm{b} + \nu_\mathrm{t} = 4(N_\mathrm{b} + N_\mathrm{t} - 1) + \tilde{\nu}, \tag{3}$$

where $\tilde{\nu} = \tilde{\nu}_\mathrm{b} + \tilde{\nu}_\mathrm{t}$.

In our theory, the system can be described using four indices $\{N_\mathrm{b}, \tilde{\nu}_\mathrm{b}; N_\mathrm{t}, \tilde{\nu}_\mathrm{t}\}$ in the quantum Hall regime, which determines the filling factor of each layer and the total filling factor.

The total energy per area E_{tot} of the system in the quantum Hall regime can be decomposed into the following contributions:

$$E_{\mathrm{tot}}[N_\mathrm{b}, \tilde{\nu}_\mathrm{b}; N_\mathrm{t}, \tilde{\nu}_\mathrm{t}] = E_{\mathrm{LL}} + E_\mathrm{C} + E_\mathrm{X}. \tag{4}$$

First, E_{LL} accounts for the single-particle energies of the occupied LLs,

$$E_{\mathrm{LL}} = \sum_{i=\mathrm{b,t}} \left\{ \sum_{N=-\infty}^{N_i-1} 4\varepsilon_{\mathrm{LL}}(N) n_0 + \varepsilon_{\mathrm{LL}}(N_i) \tilde{\nu}_i n_0 \right\}, \tag{5}$$

where $\varepsilon_{\mathrm{LL}}(N) = \mathrm{sgn}(N) v_\mathrm{F} \sqrt{2\hbar e B |N|}$ is the energy of the Nth LL, with v_F being the velocity of the Dirac fermion.

Second, E_C describes the classical electrostatic energy for the charge distribution of the bilayer

$$E_\mathrm{C} = \frac{U}{2}(n_\mathrm{b} - n_\mathrm{t}) - \frac{e^2 d_{\mathrm{GG}}}{2\varepsilon_{\mathrm{GG}}} n_\mathrm{t} n_\mathrm{b} = E_0[\tilde{D}(\nu_\mathrm{b} - \nu_\mathrm{t}) - \nu_\mathrm{t}\nu_\mathrm{b}], \tag{6}$$

where $U = eDd_{\mathrm{GG}}/\varepsilon_{\mathrm{GG}}$ is the layer potential difference generated by the displacement field D, $e > 0$ is the elementary charge, d_{GG} is the interlayer distance and $\varepsilon_{\mathrm{GG}}$ is the dielectric constant. The second term in E_C arises from the capacitor energy of the charged bilayer, where the capacitance per area is $C_{\mathrm{GG}} = \varepsilon_{\mathrm{GG}}/d_{\mathrm{GG}}$. In equation (6), $E_0 = e^2 n_0^2/(2C_{\mathrm{GG}})$ sets a scale for the electrostatic energy, and $\tilde{D}$ is given by

$$\tilde{D} = \frac{D}{en_0} = \frac{D}{B} \Big/ \left(\frac{e^2}{h}\right), \tag{7}$$

where $\tilde{D}$ is dimensionless.

Finally, E_X is the intralayer exchange energy of the filled LLs. We assume that E_X takes the following form:

$$E_\mathrm{X} = \sum_{i=\mathrm{b,t}} \left\{ (4 - \tilde{\nu}_i)\varepsilon_\mathrm{X}(N_i - 1) + \tilde{\nu}_i \varepsilon_\mathrm{X}(N_i) \right\}. \tag{8}$$

The assumption is as follows. Because $\tilde{\nu}_i$ flavours occupy LLs with index $N \le N_i$, they contribute exchange energy of $\tilde{\nu}_i \varepsilon_\mathrm{X}(N_i)$, with $\varepsilon_\mathrm{X}(N_i)$ being the exchange energy per flavour. A similar reasoning leads to the other term $(4 - \tilde{\nu}_i)\varepsilon_\mathrm{X}(N_i - 1)$. We assume that the exchange energy is additive regarding the flavour degree of freedom, which is reasonable because of the approximate SU(4) symmetry of graphene in the quantum Hall regime.

The atomic-scale interactions in graphene are known to break the SU(4) symmetry in the spin and valley flavour space and act as perturbations to lift degeneracies between states that would otherwise be related by SU(4) symmetry. However, their energy scale compared with the dominant SU(4) symmetric long-range Coulomb interaction is smaller by a factor of a_0/l_B, where a_0 is the monolayer graphene lattice constant and l_B is the magnetic length[40,41]. For a typical magnetic length of 10 T, $a_0/l_B \approx 0.03$. Therefore, the total energy is mainly contributed by the SU(4) symmetric long-range Coulomb interaction. This is why the exchange energy is approximately additive with respect to the flavour degree of freedom, as the long-range Coulomb interaction dominates.

Motivated by the experimental observation, we focus on the case that both ν_b and ν_t are integers. Our experiment shows no evidence of an interlayer coherent state. Accordingly, we theoretically consider

quantum Hall states that preserve the layer U(1) symmetry, so that the particle numbers in each layer are conserved. For this class of states, the absence of interlayer coherence causes the interlayer exchange interaction to vanish. Meanwhile, E_C represents the overall effect of intralayer and interlayer electrostatic energies.

We note that the Zeeman energy is not included in equation (4). We discuss the effect of the spin ordering and Zeeman energy separately.

Critical displacement fields. At a critical displacement field for the LL crossing, the energies of two different states become degenerate. When the crossing checkerboard is formed, the filling factor within each layer changes by 1 at each critical displacement field. Therefore, we compare the energies of two states described respectively by $\{N_b, \tilde{\nu}_b - 1; N_t, \tilde{\nu}_t + 1\}$ and $\{N_b, \tilde{\nu}_b; N_t, \tilde{\nu}_t\}$,

$$\begin{aligned} & E_{\mathrm{tot}}\left[N_b, \tilde{\nu}_b - 1; N_t, \tilde{\nu}_t + 1\right] - E_{\mathrm{tot}}\left[N_b, \tilde{\nu}_b; N_t, \tilde{\nu}_t\right] \\ & = \left[\mathcal{E}_{\mathrm{LL}}(N_t) - \mathcal{E}_{\mathrm{LL}}(N_b)\right] n_0 + E_0\left[-2\tilde{D} + 1 + 4(N_t - N_b) + \tilde{\nu}_t - \tilde{\nu}_b\right] \\ & + \left[\mathcal{E}_{\mathrm{X}}(N_t) - \mathcal{E}_{\mathrm{X}}(N_t - 1))\right] - \left[\mathcal{E}_{\mathrm{X}}(N_b) - \mathcal{E}_{\mathrm{X}}(N_b - 1))\right]. \end{aligned} \tag{9}$$

By setting equation (9) to zero, we obtain the critical displacement field, which is given by

$$\tilde{D}^{(c)}_{N_b,N_t}\left(\tilde{\nu}_b, \tilde{\nu}_t \leftrightarrow \tilde{\nu}_b - 1, \tilde{\nu}_t + 1\right) = \tilde{D}^{(0)}_{N_b,N_t} + \frac{\tilde{\nu}_t - \tilde{\nu}_b + 1}{2}, \tag{10}$$

where $\tilde{D}^{(0)}_{N_b,N_t}$ is independent of $\tilde{\nu}_b$ and $\tilde{\nu}_t$,

$$\begin{aligned} \tilde{D}^{(0)}_{N_b,N_t} = & \left\{\left[\mathcal{E}_{\mathrm{LL}}(N_t) - \mathcal{E}_{\mathrm{LL}}(N_b)\right] n_0 + \left[\mathcal{E}_{\mathrm{X}}(N_t) - \mathcal{E}_{\mathrm{X}}(N_t - 1))\right]\right. \\ & \left. - \left[\mathcal{E}_{\mathrm{X}}(N_b) - \mathcal{E}_{\mathrm{X}}(N_b - 1))\right]\right\}/2E_0 + 2(N_t - N_b). \end{aligned} \tag{11}$$

Here, the dimensionless $\tilde{D}$ and the physical D are related through equation (7). $\tilde{D}^{(0)}_{N_b,N_t}$ is the displacement field at the centre of the checkerboard labelled by (N_b, N_t). Equation (10) correctly captures the quantized interval of critical displacement fields within each LL-crossing checkerboard, as listed in Table 1.

Spin ordering and Zeeman effect. The effect of Zeeman energy, which is not taken into account in the above derivation, depends on the spin ordering at each filling factor. Meanwhile, the spin and valley ordering in the quantum Hall regime of graphene is determined by microscopic physics down to the atomic scale. Depending on the spin polarization at each filling factor, the Zeeman energy can shift the critical displacement fields and lead to corrections on the quantized interval. However, for Sample-S15 and Sample-S37, the intervals of critical displacement fields within each checkerboard display descent quantized value, as if the Zeeman energy does not play a role. One scenario for this observation is that the charge transfer between the two layers at the critical displacement fields is spin-conserved; the Zeeman energy of the system does not change across the transition, which leads to no correction on the critical displacement fields.

The Zeeman energy should be identical across different samples under the same magnetic field; however, atomic-scale interactions may vary between samples owing to differences in the screening environment, as demonstrated by previous experiments. Specifically, scanning tunnelling microscopy studies of charge-neutral graphene in strong magnetic fields have revealed a Kekulé-distorted ground state[42], whereas non-local spin and charge transport measurements on double-encapsulated graphene with a higher effective dielectric constant have identified an antiferromagnetic ground state[43]. A theoretical mechanism that takes into account LL mixing shows that the atomic-scale interactions are indeed sensitive to the dielectric environment, providing an explanation of the above seemingly conflicting observations[44]. In our case, the screening environment can vary across samples owing to differences in the thickness of the h-BN-encapsulating layers, which can lead to distinct atomic-scale interactions and spin orderings.

Reporting summary

Further information on research design is available in the Nature Portfolio Reporting Summary linked to this article.

Data availability

The data that support the findings of this study are available via Zenodo at https://doi.org/10.5281/zenodo.17149216 (ref. 45).

References

1. van Wees, B. J. et al. Quantized conductance of point contacts in a two-dimensional electron gas. *Phys. Rev. Lett.* **60**, 848–850 (1988).
2. Wharam, D. A. et al. One-dimensional transport and the quantisation of the ballistic resistance. *J. Phys. C* **21**, L209 (1988).
3. Dean, C. C. & Pepper, M. The transition from two- to one-dimensional electronic transport in narrow silicon accumulation layers. *J. Phys. C* **15**, L1287 (1982).
4. Thornton, T. J., Pepper, M., Ahmed, H., Andrews, D. & Davies, G. J. One-dimensional conduction in the 2D electron gas of a GaAs-AlGaAs heterojunction. *Phys. Rev. Lett.* **56**, 1198–1201 (1986).
5. Shapiro, S. Josephson currents in superconducting tunneling: the effect of microwaves and other observations. *Phys. Rev. Lett.* **11**, 80–82 (1963).
6. Grimes, C. C. & Shapiro, S. Millimeter-wave mixing with Josephson junctions. *Phys. Rev.* **169**, 397–406 (1968).
7. Klitzing, K. V., Dorda, G. & Pepper, M. New method for high-accuracy determination of the fine-structure constant based on quantized Hall resistance. *Phys. Rev. Lett.* **45**, 494–497 (1980).
8. Kane, C. L. & Mele, E. J. Quantum spin Hall effect in graphene. *Phys. Rev. Lett.* **95**, 226801 (2005).
9. Haldane, F. D. M. Model for a quantum Hall effect without Landau levels: condensed-matter realization of the 'parity anomaly'. *Phys. Rev. Lett.* **61**, 2015–2018 (1988).
10. Chang, C.-Z. et al. Experimental observation of the quantum anomalous Hall effect in a magnetic topological insulator. *Science* **340**, 167–170 (2013).
11. Provost, J. & Vallee, G. Riemannian structure on manifolds of quantum states. *Commun. Math. Phys.* **76**, 289–301 (1980).
12. Han, J. et al. Room-temperature flexible manipulation of the quantum-metric structure in a topological chiral antiferromagnet. *Nat. Phys.* **20**, 1110–1117 (2024).
13. Wang, Y. et al. Quantum Hall phase in graphene engineered by interfacial charge coupling. *Nat. Nanotechnol.* **17**, 1272–1279 (2022).
14. Ribeiro-Palau, R. et al. Quantum Hall resistance standard in graphene devices under relaxed experimental conditions. *Nat. Nanotechnol.* **10**, 965–971 (2015).
15. Chuang, I. & Nielsen, M. *Quantum Computation and Quantum Information* (Cambridge Univ. Press, 2010).
16. Sanchez-Yamagishi, J. D. et al. Quantum Hall effect, screening, and layer-polarized insulating states in twisted bilayer graphene. *Phys. Rev. Lett.* **108**, 076601 (2012).
17. Yuan, Y. et al. Interplay of Landau quantization and interminivalley scatterings in a weakly coupled moiré superlattice. *Nano Lett.* **24**, 6722–6729 (2024).
18. Slizovskiy, S. et al. Out-of-plane dielectric susceptibility of graphene in twistronic and Bernal bilayers. *Nano Lett.* **21**, 6678–6683 (2021).
19. Li, Q. et al. Strongly coupled magneto-exciton condensates in large-angle twisted double bilayer graphene. *Nat. Commun.* **15**, 5065 (2024).

20. Pezzini, S. et al. 30-twisted bilayer graphene quasicrystals from chemical vapor deposition. *Nano Lett.* **20**, 3313–3319 (2020).
21. Cao, Y. et al. Unconventional superconductivity in magic-angle graphene superlattices. *Nature* **556**, 43–50 (2018).
22. Tang, H. et al. On-chip multi-degree-of-freedom control of two-dimensional materials. *Nature* **632**, 1038–1044 (2024).
23. Liu, C. et al. Designed growth of large bilayer graphene with arbitrary twist angles. *Nat. Mater.* **21**, 1263–1268 (2022).
24. Xie, Y. et al. Fractional Chern insulators in magic-angle twisted bilayer graphene. *Nature* **600**, 439–443 (2021).
25. Cao, Y. et al. Correlated insulator behaviour at half-filling in magic-angle graphene superlattices. *Nature* **556**, 80–84 (2018).
26. de Vries, F. K. et al. Combined minivalley and layer control in twisted double bilayer graphene. *Phys. Rev. Lett.* **125**, 176801 (2020).
27. Rickhaus, P. et al. Correlated electron-hole state in twisted double-bilayer graphene. *Science* **373**, 1257–1260 (2021).
28. Yao, W. et al. Quasicrystalline 30° twisted bilayer graphene as an incommensurate superlattice with strong interlayer coupling. *Proc. Natl Acad Sci. USA* **115**, 6928–6933 (2018).
29. Ahn, S. J. et al. Dirac electrons in a dodecagonal graphene quasicrystal. *Science* **361**, 782–786 (2018).
30. Koren, E. et al. Coherent commensurate electronic states at the interface between misoriented graphene layers. *Nat. Nanotechnol.* **11**, 752–757 (2016).
31. Cohen, L. A. et al. Nanoscale electrostatic control in ultra-clean van der Waals heterostructures by local anodic oxidation of graphite gates. *Nat. Phys.* **19**, 1502–1508 (2023).
32. Wang, L. et al. One-dimensional electrical contact to a two-dimensional material. *Science* **342**, 614–617 (2013).
33. Zhang, Y. et al. Direct observation of a widely tunable bandgap in bilayer graphene. *Nature* **459**, 820–823 (2009).
34. Ju, L. et al. Tunable excitons in bilayer graphene. *Science* **358**, 907–910 (2017).
35. Yang, K. et al. Unconventional correlated insulator in CrOCl-interfaced Bernal bilayer graphene. *Nat. Commun.* **14**, 2136 (2023).
36. Taychatanapat, T. & Jarillo-Herrero, P. Electronic transport in dual-gated bilayer graphene at large displacement fields. *Phys. Rev. Lett.* **105**, 166601 (2010).
37. Liu, Y. et al. Evolution of the 7/2 fractional quantum Hall state in two-subband systems. *Phys. Rev. Lett.* **107**, 266802 (2011).
38. Bennett, J. S. et al. Precision magnetometers for aerospace applications: a review. *Sensors* **21**, 5568 (2021).
39. Reif, B., Ashbrook, S. E., Emsley, L. & Hong, M. Solid-state NMR spectroscopy. *Nat. Rev. Methods Primers* **1**, 2 (2021).
40. Kharitonov, M. Phase diagram for the $\nu = 0$ quantum Hall state in monolayer graphene. *Phys. Rev. B* **85**, 155439 (2012).
41. Wu, F., Sodemann, I., Araki, Y., MacDonald, A. H. & Jolicoeur, T. SO(5) symmetry in the quantum Hall effect in graphene. *Phys. Rev. B* **90**, 235432 (2014).
42. Liu, X. et al. Visualizing broken symmetry and topological defects in a quantum Hall ferromagnet. *Science* **375**, 321–326 (2022).
43. Young, A. F. et al. Tunable symmetry breaking and helical edge transport in a graphene quantum spin Hall state. *Nature* **505**, 528–532 (2014).
44. Wei, N., Xu, G., Villadiego, I. S. & Huang, C. Landau-level mixing and SU(4) symmetry breaking in graphene. *Phys. Rev. Lett.* **134**, 046501 (2025).
45. Dong, Z. et al. Quantized Landau-level crossing checkerboards for cryogenic magnetometry. *Zenodo* https://doi.org/10.5281/zenodo.17149216 (2025).

Acknowledgements

We appreciate helpful discussions with X. Dai. This work is supported by the National Key R&D Program of China (2022YFA1203903, 2022YFA1402400) and the National Natural Science Foundation of China (NSFC) (grant nos. 92265203, 12450003, 12034011, U23A6004, 12374185, 12374168, 62204145, 92565302 and 12274333). Z.V.H. acknowledges the support of the Fund for Shanxi '1331 Project' Key Subjects Construction. B.D and J. Zhang acknowledge support from the Quantum Science and Technology-National Science and Technology Major Project (grant no. 2021ZD0302003). K.W. and T.T. acknowledge support from the JSPS KAKENHI (grant nos. 20H00354 and 23H02052) and World Premier International Research Center Initiative (WPI), MEXT, Japan. We thank the WM1 of the Steady High Magnetic Field Facility, CAS (https://cstr.cn/31125.02.SHMFF.WM1) for the assistance on the experiment.

Author contributions

Z.V.H. and J. Zhang conceived of the experiment and supervised the overall project. B.D. and K.Z. performed the device fabrications and measurements. F.W. proposed the theoretical mechanism. Z.W. and C.X contributed to high-magnetic-field measurements. K.W. and T.T. provided high-quality h-BN bulk crystals. Z.V.H., B.D., K.Z., F.W., J.L., J. Zhao, C.Z. and J. Zhang analysed the experimental data. Z.V.H., B.D. and K.Z. wrote the paper, with discussions and inputs from all authors.

Competing interests

The authors declare no competing interests.

Additional information

Supplementary information The online version contains supplementary material available at https://doi.org/10.1038/s44460-025-00018-8.

Correspondence and requests for materials should be addressed to Jianting Zhao, Fengcheng Wu, Jing Zhang or Zheng Vitto Han.

Peer review information *Nature Sensors* thanks Jie Shen and the other, anonymous, reviewer(s) for their contribution to the peer review of this work. Peer reviewer reports are available.

nature portfolio

Corresponding author(s): Jianting ZHAO, Fengcheng WU, Jing ZHANG, Zheng Vitto Han

Last updated by author(s): 2025-Nov-17

Reporting Summary

Nature Portfolio wishes to improve the reproducibility of the work that we publish. This form provides structure for consistency and transparency in reporting. For further information on Nature Portfolio policies, see our Editorial Policies and the Editorial Policy Checklist.

Statistics

For all statistical analyses, confirm that the following items are present in the figure legend, table legend, main text, or Methods section.

n/a	Confirmed
☐	☒ The exact sample size (*n*) for each experimental group/condition, given as a discrete number and unit of measurement
☐	☒ A statement on whether measurements were taken from distinct samples or whether the same sample was measured repeatedly
☒	☐ The statistical test(s) used AND whether they are one- or two-sided *Only common tests should be described solely by name; describe more complex techniques in the Methods section.*
☒	☐ A description of all covariates tested
☐	☒ A description of any assumptions or corrections, such as tests of normality and adjustment for multiple comparisons
☐	☒ A full description of the statistical parameters including central tendency (e.g. means) or other basic estimates (e.g. regression coefficient) AND variation (e.g. standard deviation) or associated estimates of uncertainty (e.g. confidence intervals)
☒	☐ For null hypothesis testing, the test statistic (e.g. *F*, *t*, *r*) with confidence intervals, effect sizes, degrees of freedom and *P* value noted *Give P values as exact values whenever suitable.*
☒	☐ For Bayesian analysis, information on the choice of priors and Markov chain Monte Carlo settings
☒	☐ For hierarchical and complex designs, identification of the appropriate level for tests and full reporting of outcomes
☒	☐ Estimates of effect sizes (e.g. Cohen's *d*, Pearson's *r*), indicating how they were calculated

Our web collection on statistics for biologists contains articles on many of the points above.

Software and code

Policy information about availability of computer code

Data collection	Data collection was performed using a custom-built program developed in LabVIEW 2014.
Data analysis	Data was analyzed using Matlab 2020.

For manuscripts utilizing custom algorithms or software that are central to the research but not yet described in published literature, software must be made available to editors and reviewers. We strongly encourage code deposition in a community repository (e.g. GitHub). See the Nature Portfolio guidelines for submitting code & software for further information.

Data

Policy information about availability of data

All manuscripts must include a data availability statement. This statement should provide the following information, where applicable:

- Accession codes, unique identifiers, or web links for publicly available datasets
- A description of any restrictions on data availability
- For clinical datasets or third party data, please ensure that the statement adheres to our policy

The data that support the findings of this study are available via Zenodo at https://doi.org/10.5281/zenodo.17149216

Research involving human participants, their data, or biological material

Policy information about studies with human participants or human data. See also policy information about sex, gender (identity/presentation), and sexual orientation and race, ethnicity and racism.

Reporting on sex and gender	No human participants, human data, or biological materials were involved in this study. The research focuses solely on magnetotransport measurements of twisted graphene devices; therefore, sex and gender variables were not collected, analyzed, or applicable.
Reporting on race, ethnicity, or other socially relevant groupings	This study did not involve human participants. As such, no socially relevant categorizations—including race, ethnicity, socioeconomic status, or related demographic variables—were collected or considered.
Population characteristics	Not applicable. No human subjects or biological materials were involved, and no population-level data were collected.
Recruitment	Not applicable. No human participants were recruited for this study, which exclusively involves solid-state quantum devices and their physical transport measurements.
Ethics oversight	Ethics approval was not required. This study does not include human participants, human data, animals, or biological specimens.

Note that full information on the approval of the study protocol must also be provided in the manuscript.

Field-specific reporting

Please select the one below that is the best fit for your research. If you are not sure, read the appropriate sections before making your selection.

☐ Life sciences ☐ Behavioural & social sciences ☒ Ecological, evolutionary & environmental sciences

For a reference copy of the document with all sections, see nature.com/documents/nr-reporting-summary-flat.pdf

Ecological, evolutionary & environmental sciences study design

All studies must disclose on these points even when the disclosure is negative.

Study description	This study investigates quantum magnetotransport phenomena in large-angle twisted graphene devices, focusing on quantized Landau-level–crossing checkerboards and their application as a new paradigm for cryogenic quantum magnetometry. The measurements were performed on microfabricated graphene/h-BN heterostructures under high magnetic fields and low temperatures.
Research sample	The samples consist exclusively of solid-state devices: mechanically exfoliated monolayer graphene and hexagonal boron nitride (h-BN) assembled into van der Waals heterostructures. No biological, ecological, or human-derived samples were used.
Sampling strategy	No statistical methods were used to predetermine sample size. The study focuses on deterministic physical properties of microfabricated twisted-graphene devices rather than population-level variability. Sample sizes were chosen based on standard practices in quantum transport studies, where reproducibility across independently fabricated devices is used to validate robustness. Multiple devices with similar geometries and twist configurations were fabricated and measured. All key phenomena—including the quantized Landau-level–crossing checkerboards and their magnetic-field scaling—were consistently reproduced across these devices and across multiple measurement cooldowns. This reproducibility demonstrates that the chosen sample size is sufficient to support the study's conclusions.
Data collection	Data were collected using low-temperature magnetotransport measurements performed in two cryogenic systems: (1) a 30 T water-cooled magnet at the Steady High Magnetic Field Facility (CAS), and (2) an Oxford Instruments cryostat with a base temperature of 1.5 K and a superconducting magnet providing fields up to 12 T. Electrical resistance and conductance were measured using standard low-frequency lock-in techniques. Gate-voltage sweeps, magnetic-field control, and synchronized data acquisition were automated through a custom-built LabVIEW 2014 program. All measurement procedures and raw data recordings were carried out by trained members of the research team.
Timing and spatial scale	Data collection was conducted from July 20, 2022, to August 24, 2025. Measurements were performed following a "sample preparation and testing in parallel" approach, where there was no fixed schedule for sample replacement or measurement frequency. Instead, the timing and duration of measurements were adapted to the specific characteristics of each sample. The spatial scale of data collection corresponded to the micrometer-scale active regions of individual graphene devices, typically covering areas of ~10 µm × 10 µm per device. Measurements were performed at various temperatures and magnetic field strengths according to the sample's properties, with the measurement detail and conditions adjusted to capture key low-temperature transport behaviors. All experiments were conducted in a low-temperature cryostat system, providing high spatial and temporal resolution for the investigation of intrinsic electronic phenomena.

Data exclusions	No data were excluded from the analyses. All measured datasets from the prepared graphene devices were included in the study, as each measurement was selected based on sample-specific characteristics and measurement conditions rather than predefined exclusion criteria.
Reproducibility	To verify the reproducibility of the experimental findings, multiple graphene devices were measured under similar fabrication and testing conditions. All samples exhibited quantum oscillations and regions of quantized Landau level crossings in low-temperature, high-magnetic-field measurements, confirming the robustness of these phenomena. Among the measured devices, only two samples displayed uniform 4×4 checkerboard Landau level crossings as described in the main text, while other samples showed non-uniform Landau level crossings. Nevertheless, the quantized Landau level crossing regions were consistently observed across all samples, and all devices could be reliably used for low-temperature, high-magnetic-field transport measurements.
Randomization	Randomization is not applicable. The study focuses on deterministic physical properties of fabricated solid-state devices.
Blinding	Blinding is not relevant, as no human or biological subjects were involved and data interpretation is not affected by observer bias.

Did the study involve field work? ☒ Yes ☐ No

Field work, collection and transport

Field conditions	All measurements were performed under controlled laboratory conditions. Most experiments were conducted using a low-temperature Oxford cryostat system at temperatures down to 1.5 K and magnetic fields up to 12 T. Additionally, some samples were measured in a 30 T water-cooled magnet at the Steady High Magnetic Field Facility (Chinese Academy of Sciences) to investigate transport properties under ultra-high magnetic fields. No environmental factors such as rainfall or ambient temperature fluctuations affected the measurements, as all experiments were carried out in shielded, cryogenically controlled environments. Sample-specific parameters, including temperature, magnetic field strength, and measurement duration, were adjusted according to device characteristics to capture quantum oscillations and Landau level crossings effectively.
Location	Experiments were conducted in laboratory facilities at Shanxi University, Taiyuan, China and Liaoning Academy of Materials, Shenyang, China. Low-temperature measurements up to 12 T were performed in the university's laboratory using an Oxford cryostat system. Additional high-magnetic-field measurements up to 30 T were conducted at the Steady High Magnetic Field Facility, Chinese Academy of Sciences, Hefei, China.
Access & import/export	All samples used in this study were fabricated and tested in laboratory facilities at Shanxi University, Liaoning Academy of Materials and the Steady High Magnetic Field Facility (CAS). No environmental or field sampling was involved. All materials and devices were handled, transported, and used in accordance with institutional safety regulations and national laws governing the fabrication and transfer of electronic materials. No import or export of biological or hazardous materials was required, and no special permits were necessary for the materials or equipment used in this study.
Disturbance	The study involved laboratory-based measurements on fabricated graphene devices and did not cause any environmental or ecological disturbance. All experimental procedures were performed in controlled cryogenic and magnetically shielded environments, ensuring that the laboratory operation, sample handling, and measurement processes had minimal impact on the surrounding environment or personnel.

Reporting for specific materials, systems and methods

We require information from authors about some types of materials, experimental systems and methods used in many studies. Here, indicate whether each material, system or method listed is relevant to your study. If you are not sure if a list item applies to your research, read the appropriate section before selecting a response.

Materials & experimental systems

n/a	Involved in the study
☒	☐ Antibodies
☒	☐ Eukaryotic cell lines
☒	☐ Palaeontology and archaeology
☒	☐ Animals and other organisms
☒	☐ Clinical data
☒	☐ Dual use research of concern
☒	☐ Plants

Methods

n/a	Involved in the study
☒	☐ ChIP-seq
☒	☐ Flow cytometry
☒	☐ MRI-based neuroimaging

Plants

Seed stocks	*Report on the source of all seed stocks or other plant material used. If applicable, state the seed stock centre and catalogue number. If plant specimens were collected from the field, describe the collection location, date and sampling procedures.*
Novel plant genotypes	*Describe the methods by which all novel plant genotypes were produced. This includes those generated by transgenic approaches, gene editing, chemical/radiation-based mutagenesis and hybridization. For transgenic lines, describe the transformation method, the number of independent lines analyzed and the generation upon which experiments were performed. For gene-edited lines, describe the editor used, the endogenous sequence targeted for editing, the targeting guide RNA sequence (if applicable) and how the editor was applied.*
Authentication	*Describe any authentication procedures for each seed stock used or novel genotype generated. Describe any experiments used to assess the effect of a mutation and, where applicable, how potential secondary effects (e.g. second site T-DNA insertions, mosiacism, off-target gene editing) were examined.*